RESEARCH ARTICLE SUMMARY

MOLECULAR BIOLOGY

WAPL functions as a rheostat of Protocadherin isoform diversity that controls neural wiring

Lea Kiefer†, Anna Chiosso†, Jennifer Langen†, Alex Buckley†, Simon Gaudin, Sandy M. Rajkumar‡, Gabrielle Isabelle F. Servito‡, Elizabeth S. Cha, Akshara Vijay, Albert Yeung, Adan Horta, Michael H. Mui, Daniele Canzio*

INTRODUCTION: The establishment of neural connectivity patterns requires the ability of individual neurons to distinguish self from nonself. In mammals, clustered Protocadherin (Pcdh) genes encode cell surface molecular "identifiers" (i.e., barcodes) that allow neural "self/nonself" discrimination: Neurites from the same cell carrying identical Pcdh barcodes recognize and repel each other, whereas neurites from different cells carrying distinct Pcdh barcodes do not. In mice, there are 116 Pcdh genes, 58 on each of the two homologous chromosomes, organized into three tandemly arranged clusters (α, β, and γ). Different neural types express distinct repertoires of Pcdh genes to instruct their wiring processes. The most noteworthy examples of this behavior are the deterministic expression of a single Pcdh gene in serotonergic neurons (5-HTs) and the stochastic expression of a few Pcdh genes in olfactory sensory neurons (OSNs). Deterministic expression of Pcdhαc2 provides 5-HTs with a single, shared barcode. Using this mechanism, neurites from the same cell not only recognize and repel self, but also neurites from other 5-HTs, thus favoring nonoverlapping tiled projections of their axons throughout the brain. By contrast, stochastic and combinatorial expression of distinct repertoires of Pcdh genes provides each OSN with a unique barcode. The generation of this barcoding diversity enables convergence of OSN axons into tightly packed, overlapping structures. These observations pose a fundamental question: How do neurons choose the correct number (and type) of Pcdh genes to support their wiring needs?

RATIONALE: The genomic architecture of Pcdh genes poses a fundamental regulatory challenge: cis-regulatory mechanisms must overcome genomic-proximity biases imposed by the linear arrangement of Pcdh promoters relative to distal enhancers. These mechanisms must be regulated differently in distinct cell types. For instance, in 5-HTs, choice of the Pcdhαc2 gene is genomic-distance biased, because its promoter is the most enhancer-proximal promoter in the Pcdhα cluster. However, in OSNs, genomic-distance biases in promoter choice are erased in favor of random selection. Previous studies have suggested a role for the DNA translocase cohesin in regulating Pcdh expression by mediating enhancer-promoter interactions. Building upon these studies, we hypothesized that differential regulation of cohesin activity could be a potential mechanism by which neurons achieve the Pcdh expression programs that support their wiring patterns.

RESULTS: By genetically targeting components of the cohesin complex in 5-HTs and OSNs, we revealed that neural type–specific Pcdh expression and axonal behavior depend on the activity of cohesin and its unloader, WAPL (wings apart-like protein homolog). Given the linear arrangement of Pcdh genes, high WAPL in 5-HTs limits cohesin translocation, thereby favoring the expression of the enhancer-proximal Pcdhαc2 isoform in all cells and ultimately constraining axon arrangements to a tiling pattern. Conditional deletion of WAPL in 5-HTs resulted in loss of Pcdhαc2 expression and disruption of axon tiling. By contrast, we found that low WAPL in OSNs enables cohesin translocation along the locus. Using this mechanism, cohesin increases the probability of contacts between the enhancers and the more distal Pcdh promoters, thereby enabling stochastic expression of a larger repertoire of Pcdh isoforms and ultimately driving axon convergence and assembly of olfactory circuits. In OSNs, conditional ablation of Rad21, an essential subunit of the cohesin complex, resulted in loss of Pcdh isoform diversity and gain of the biased expression of the enhancer-proximal Pcdhαc2 gene. Thus, Rad21 ablation turned the Pcdh expression profile of OSNs into one reminiscent of 5HTs. Loss of Pcdh diversity by Rad21 deletion resulted in disruption of OSN axon convergence. Therefore, by countering enhancer-promoter genomic proximity biases, neural type–specific regulation of cohesin activity by WAPL tunes Pcdh isoform diversity and enables distinct modes of neuronal wiring and circuit assembly.

CONCLUSION: We propose a model in which WAPL functions as a rheostat of cohesin processivity on DNA to enable structural and transcriptional modularity of the Pcdh gene cluster required to establish different patterns of neural connectivity during brain development. More broadly, our data suggest a new class of regulatory principles for genes organized in clusters in which cells use rheostat-operating logics to overcome distance biases in gene selection. We speculate that rheostats are solutions to the challenges imposed by the complex architectures of these gene clusters that generate the transcriptional diversity critical for cellular and functional diversification. ■

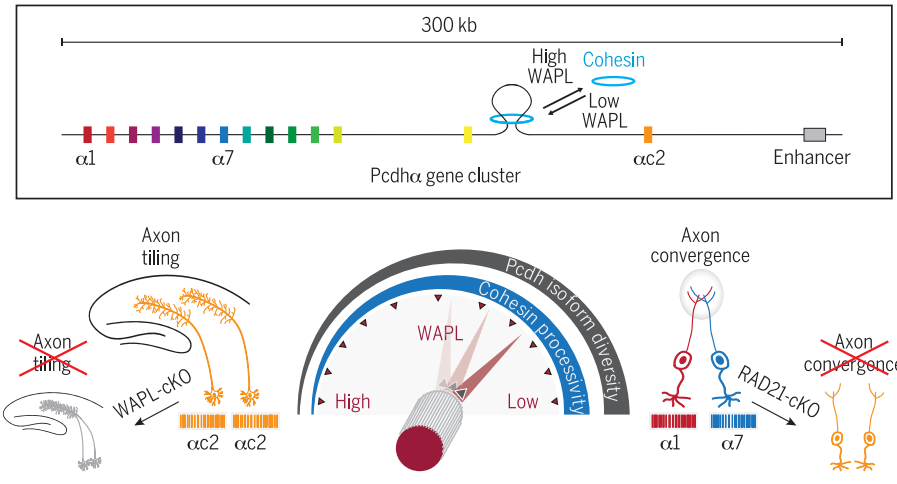

WAPL functions as a rheostat of cohesin processivity and Pcdh isoform diversity. In 5-HTs, high WAPL limits cohesin translocation, which favors Pcdhαc2 expression and axon tiling. Loss of WAPL results in 5-HT tiling defects. In OSNs, low WAPL enables cohesin translocation, which favors Pcdh isoform diversity and axon convergence. Loss of Rad21 (a cohesin subunit) results in OSN convergence defects. Only the Pcdhα gene cluster is shown.

The list of author affiliations is available in the full article online.
*Corresponding author. Email: daniele.canzio@ucsf.edu
†These authors contributed equally to this work.
‡These authors contributed equally to this work.
Cite this article as L. Kiefer *et al.*, *Science* **380**, eadf8440 (2023). DOI: 10.1126/science.adf8440

READ THE FULL ARTICLE AT
https://doi.org/10.1126/science.adf8440

RESEARCH ARTICLE

MOLECULAR BIOLOGY

WAPL functions as a rheostat of Protocadherin isoform diversity that controls neural wiring

Lea Kiefer[1,2]†, Anna Chiosso[1,2]†, Jennifer Langen[1,2,3]†, Alex Buckley[1,2,3]†, Simon Gaudin[1,2,4], Sandy M. Rajkumar[1,2]‡, Gabrielle Isabelle F. Servito[1,2]‡, Elizabeth S. Cha[1,2], Akshara Vijay[1,2], Albert Yeung[5], Adan Horta[6], Michael H. Mui[1,2], Daniele Canzio[1,2,7]*

Neural type–specific expression of clustered Protocadherin (Pcdh) proteins is essential for the establishment of connectivity patterns during brain development. In mammals, deterministic expression of the same Pcdh isoform promotes minimal overlap of tiled projections of serotonergic neuron axons throughout the brain, while stochastic expression of Pcdh genes allows for convergence of tightly packed, overlapping olfactory sensory neuron axons into targeted structures. How can the same gene locus generate opposite transcriptional programs that orchestrate distinct spatial arrangements of axonal patterns? Here, we reveal that cell type–specific Pcdh expression and axonal behavior depend on the activity of cohesin and its unloader, WAPL (wings apart–like protein homolog). While cohesin erases genomic-distance biases in Pcdh choice, WAPL functions as a rheostat of cohesin processivity that determines Pcdh isoform diversity.

The generation of cellular diversity is vital to the many functions of higher organisms, from the detection of microbes by the immune system to the ability to perceive and interpret the outside world by the central nervous system. Stochastic expression of genes organized in clusters, from immunoglobulin to the olfactory receptor to clustered Protocadherin (Pcdh) genes, represents an extraordinary example of a mechanism by which cells greatly expand their proteome repertoire to achieve unparalleled diversification (*1*–*3*). There are different challenges that these systems must overcome to promote random gene choice. While olfactory receptor gene choice relies on interchromosomal contacts (*2*, *4*), the genomic architectures of the immunoglobulin and Pcdh loci call for cis-regulatory mechanisms that overcome genomic distance biases imposed by the linear arrangement of these genes relative to their cis-regulatory elements.

In mice, there are a total of 116 clustered Pcdh genes (120 in humans), 58 on each of the two homologous chromosomes, organized into three tandemly arranged gene clusters (14 Pcdhα, 22 Pcdhβ, and 22 Pcdhγ) spanning nearly 1 million base pairs of genomic DNA (*5*, *6*) (Fig. 1A). Each cluster is regulated by cluster-specific transcriptional enhancers located downstream (3′) of the promoters, with distances between enhancers and promoters that can reach up to 600,000 base pairs (*7*, *8*) (Fig. 1A: HS5-1, HS18-22, and HS16-17 are the transcriptional enhancers of the Pcdhα, Pcdhβ, and Pcdhγ clusters, respectively).

Clustered Pcdh genes encode cell surface proteins that "barcode" individual neurons with unique identities (*3*, *9*, *10*). This mechanism allows neurons to self-recognize and self-avoid as they establish proper connections with neighboring cells during brain development (*3*, *9*, *10*). There are two broad classes of neuronal contact patterns: tiling and convergence (*11*–*13*). In mammals, neural tiling is epitomized by serotonergic neurons (5-HTs) whose axons must minimize overlap with their neighboring 5-HTs to innervate various brain regions (*14*–*16*). Tiling of 5-HT axons is achieved by the deterministic expression of only Pcdhαc2, the most HS5-1 enhancer–proximal Pcdhα gene, which conveys an identical Pcdh barcode to the cell surfaces of this class of neurons (*14*, *16*). Deletion of Pcdhαc2 results in a marked tiling defect of 5-HT projections (*14*, *16*), a self-avoidance phenotype (i.e., neurites clumping together) similar to that previously observed in starburst amacrine cells upon genetic removal of the Pcdhγ genes (*17*). Convergence is instead exemplified by olfactory sensory neurons (OSNs) whose axons expressing the same olfactory receptor (OR), but distinct repertoires of clustered Pcdh genes, must coalesce into tightly packed structures known as glomeruli (*18*–*21*). These distinct Pcdh repertoires are generated by stochastic and combinatorial Pcdh promoter choice from all three clusters (*22*, *23*), which allows individual OSNs to display different barcodes on their cell surface (*18*). Overriding Pcdh diversity by expressing high levels of specific Pcdh isoforms in all OSNs leads to axon convergence defects and disruption of glomeruli formation in the olfactory bulb (OB) (*18*).

The establishment of these two distinct mechanisms of neural wiring, tiling and convergence, by clustered Pcdh genes represents an example of how cells must be able to commit orthogonal gene regulatory logics. They must either promote genomic distance biases in favor of deterministic promoter selection to acquire the cellular uniformity required to tile, or they must overcome such biases in favor of stochasticity to generate the cellular diversity required to converge. The regulation of these contrasting gene expression processes poses a fundamental question: How can both deterministic and stochastic promoter selection arise from the same gene cluster?

Results

OSN progenitor cells display developmental biases in Pcdhαc2 promoter choice

To investigate the process underlying the regulation of neural type–specific Pcdh expression, we first focused on studying the mechanism of stochastic Pcdh promoter choice during the maturation of OSNs. The mouse olfactory epithelium (OE) is a pseudostratified tissue composed of distinct cell types that represent different neurodevelopmental stages of OSNs, all of which have finite life spans and are continuously regenerated from mitotically active stem cells within the epithelium. To determine the precise developmental stage at which Pcdh genes are chosen by individual cells, we performed single-cell RNA sequencing (RNA-seq) from an isolated wild-type (WT) OE. Using established genetic markers for the distinct cell types of the OE, we observed developmentally regulated Pcdh gene choice (Fig. 1B). Consistent with previous observations (*24*), no Pcdh expression was observed in the intracellular adhesion protein 1–positive ($Icam1^+$) cells (horizontal basal stem cells, HBCs), which represent the quiescent stem cell population of the OE, whereas all Pcdhα isoforms were stochastically expressed in postmitotic OSNs, positive for the olfactory marker protein (Omp) and negative for the growth-associated protein 43 (Gap43) (mature olfactory sensory neurons, mOSNs) (Fig. 1B). However, we observed a transcriptional bias toward choice of the Pcdhαc2 promoter over the rest of the cluster, reminiscent of the deterministic expression of Pcdhαc2 in 5-HTs. This bias was first observed in the globose basal cells, continued into early OSN precursors, and disappeared in mOSNs (Fig. 1B). Down-regulation of Pcdhαc2 in mOSNs coincided with the onset of stochastic expression of the rest of the Pcdhα promoters (Fig. 1B).

[1]Weill Institute for Neurosciences, University of California, San Francisco, San Francisco, CA 94158, USA. [2]Department of Neurology, University of California, San Francisco, San Francisco, CA 94158, USA. [3]Neuroscience Graduate Program, University of California, San Francisco, San Francisco, CA 94158, USA. [4]Ecole Normale Superieure de Lyon, 69432 Lyon, France. [5]Department of Molecular and Cell Biology, University of California, Berkeley, Berkeley, CA 94720, USA. [6]Pura Vida Investments, New York, NY 10106, USA. [7]Chan-Zuckerberg Biohub, San Francisco, CA 94158, USA.
*Corresponding author. Email: daniele.canzio@ucsf.edu
†These authors contributed equally to this work.
‡These authors contributed equally to this work.

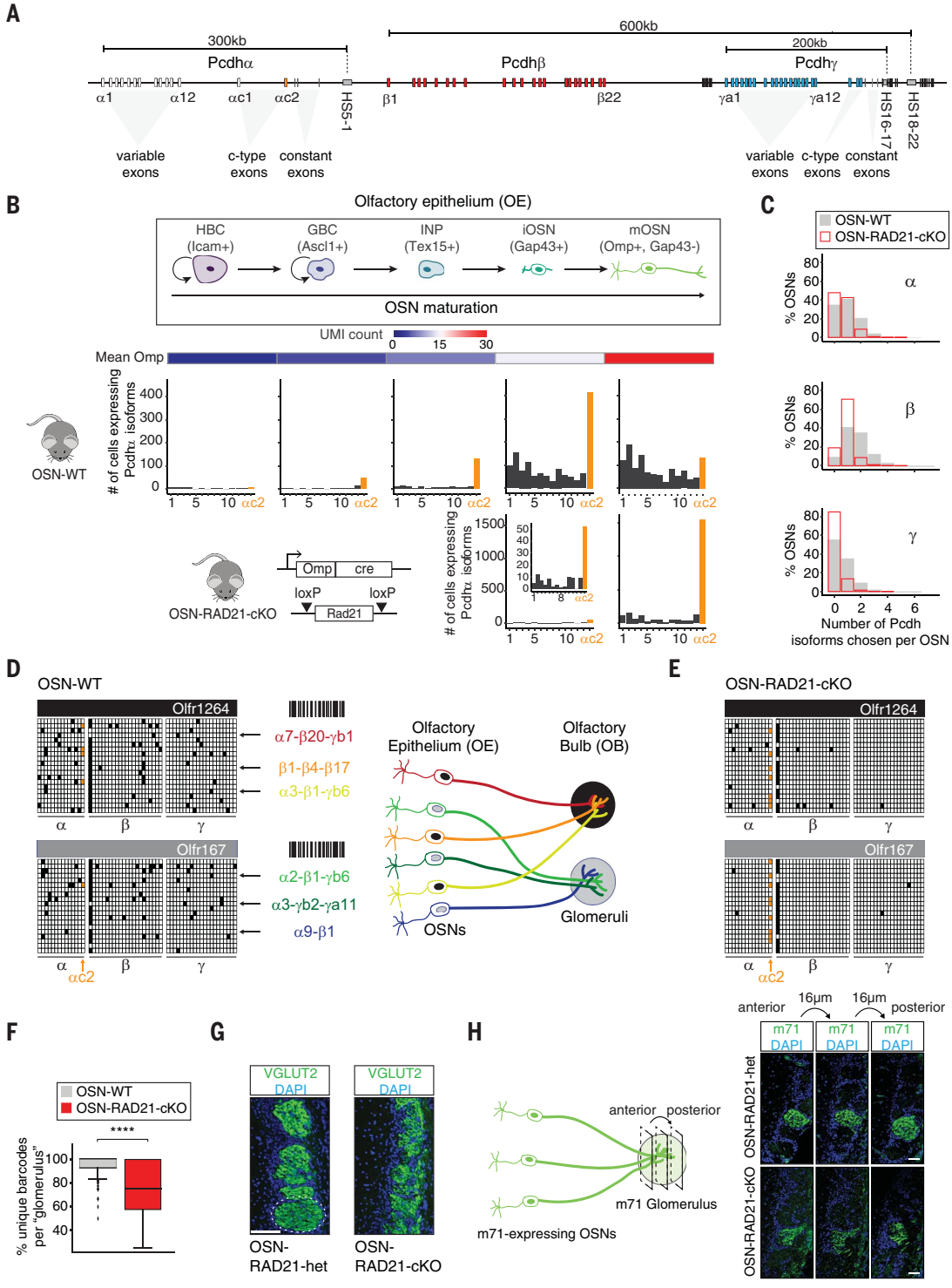

Fig. 1. Cohesin erases genomic distance biases in Pcdh promoter choice in mature OSNs. (**A**) Genomic architecture of the mouse clustered Pcdh gene locus. Pcdhα, Pcdhβ, and Pcdhγ variable 5′ exons are shown in white, red, and blue, respectively. The variable exons of the Pcdhα and Pcdhγ gene clusters are further subdivided into alternate and c-types, the latter of which includes the Pcdhαc2 gene (orange). Downstream of the Pcdhαc2 and Pcdhγc5 exons, there are three small constant exons that splice to the chosen variable exons. Cluster-specific transcriptional enhancers (HS5-1, HS16-17, and HS18-22) are shown in gray. (**B**) Pcdhα expression during OSN maturation in OSN-WT and OSN-RAD21-cKO mice. The distinct cell types that result in mOSNs are schematized on top. Heat map shows the Omp expression level. UMI, unique molecular identifier. (**C**) Histogram of the number of Pcdh isoforms chosen for expression per mOSN in OSN-WT and OSN-RAD21-cKO. Data represent one single-cell RNA-seq replicate per condition. (**D**) Left: Subset of Pcdh expression profiles from WT OSNs expressing either the OR Olfr1264 or Olfr167. Each row indicates a single cell, each column a Pcdh isoform from all three clusters. Right: Schematic of OSN axons from the OE projecting to the OB, where OSNs expressing the same OR but distinct Pcdhs converge into glomeruli. (**E**) As in (D) but from OSN-RAD21-cKO animals. (**F**) Pcdh diversity across all OSNs expressing the same OR (OSNs converging into the same "glomerulus"). (**G**) IHC against VGLUT2 in coronal sections of the OB from OSN-RAD21-het [Omp(iresCre/+);Rad21$^{fl/+}$; tdTomato$^{fl/+}$] and OSN-RAD21-cKO [Omp(iresCre/+);Rad21$^{fl/fl}$;tdTomato$^{fl/+}$]. Green, VGLUT2; blue, DAPI. Dotted white circle is an example of a glomerulus. Scale bar, 100 μm. (**H**) Left: Schematic of the coronal sections of the OB. Right: IHC against OR m71 in coronal sections from OSN-RAD21-het and OSN-RAD21-cKO. Green, m71; blue, DAPI. Scale bar, 50 μm.

Cohesin erases genomic distance biases in Pcdh promoter choice in mature OSNs

Recent studies have implicated the cohesin protein complex in regulating the expression of Pcdhα genes (*24*–*28*). Cohesin is a DNA translocase that has been proposed to regulate mammalian three-dimensional (3D) folding of the genome through a mechanism known as DNA loop extrusion. By this mechanism, cohesin loads onto DNA and extrudes chromatin until it stalls at boundary elements, usually bearing binding sites for the CCCTC-binding factor (CTCF) protein that are bound by CTCF (*29*–*32*). Within the context of the Pcdhα gene locus, cohesin has been shown to mediate long-range engagement between individual promoters and their distal HS5-1 enhancer (*24*–*28*). To determine whether cohesin functions to promote

the transcriptional switch from the deterministic expression of Pcdhαc2 to the stochastic expression of all Pcdhs in mature OSNs, we conditionally deleted the Rad21 gene. Rad21 encodes the kleisin subunit of cohesin, and its deletion renders the entire cohesin complex inactive. Deletion of Rad21 was accomplished using a Cre driver under the control of the Omp promoter [Omp(iresCre/+);Rad21$^{fl/fl}$;tdTomato$^{fl/+}$, OSN-RAD21-cKO] (fig. S1A). As shown by our single-cell RNA-seq data, Omp expression initiates in Gap43^{+} immature OSNs and continues as OSNs mature into Omp^{+},Gap43^{-} mOSNs (Fig. 1B). OSNs from WT animals were isolated by green fluorescent protein (GFP) using Omp(iresGFP/+) mice, and OSNs from OSN-RAD21-cKO were isolated using tdTomato (fig. S1B).

To filter for only mOSNs, we computationally selected Omp^{+},Gap43^{-} cells. From all cells identified as mOSNs from WT mice, 95.8% had a detectable Pcdh barcode composed of, on average, three Pcdh isoforms (Fig. 1, C and D, and fig. S1C). The probability of each individual isoform to be expressed was low, except for Pcdhβ1, which was chosen in 78.4% of mOSNs in which a Pcdh barcode was detected (Fig. 1, C and D). Our data further showed that Pcdh isoform choice was independent from the choice of ORs, demonstrating that essentially all individual OSNs bear a unique identity defined by the expression of both Pcdhs and ORs (fig. S1D).

Upon conditional deletion of the Rad21 gene, we observed a loss of Pcdh isoform diversity in all three Pcdh gene clusters and an increase in the number of mOSNs without a detectable Pcdh barcode (OSN-WT, 4.2%; OSN-RAD21-cKO, 10.4%) (Fig. 1, B to E, and fig. S1C). Although a reduction of promoter choice was observed across all three clusters, this loss appeared to follow a genomic distance dependent trend in which the most enhancer-distal promoters were the most affected (fig. S1E). Conversely, the frequency of choice of the Pcdhαc2 promoter increased ~3-fold (OSN-WT, 12.3%; OSN-RAD21-cKO, 38.0%) (Fig. 1, D and E, and fig. S1E). This genomic distance–biased expression of Pcdhα genes correlated with a decrease in chromatin contacts between the HS5-1 enhancer and the distal promoters (fig. S1F). Finally, contrary to the rest of the Pcdhβ genes, expression of Pcdhβ1 did not change (OSN-WT, 79.4%; OSN-RAD21-cKO, 78.3%), suggesting that the activation of the Pcdhβ1 promoter is cohesin independent (Fig. 1, D and E).

These data suggest that cohesin favors stochastic Pcdh promoter choice by erasing genomic distance biases in promoter selection and that, in the context of the Pcdhα gene cluster, loss of cohesin activity in mOSNs results in a Pcdh transcriptional profile reminiscent of a different class of neurons—5-HTs, where Pcdhαc2 is the only Pcdhα isoform expressed (*14*, *16*).

Cohesin activity is required for normal assembly of an olfactory map

OSN axons from the OE project to stereotypic positions in the OB, where OSNs expressing the same OR converge to form glomeruli (*33*, *34*) (Fig. 1D). Pcdh isoform diversity is necessary for OSN convergence and glomeruli formation (*18*). Given that we observed a significant loss of Pcdh isoform diversity within mOSNs expressing the same OR upon Rad21 knockout (Fig. 1F), we wondered whether Rad21 deletion resulted in any phenotypic abnormalities of the glomeruli structures. To investigate this, we compared the OB of OSN-RAD21-cKO mice with that of heterozygous littermates [Omp(iresCre/+);Rad21$^{fl/+}$;tdTomato$^{fl/+}$, OSN-RAD21-het] in which Pcdh expression was not altered relative to OSN-WT (fig. S1G). Unlike OSN-Rad21-het, glomeruli structures were disrupted throughout the OB in OSN-RAD21-cKO mice, as assayed by staining for the vesicular glutamate transporter 2 (VGLUT2) (Fig. 1G). Although we cannot exclude that this effect was caused by additional changes in gene expression upon Rad21 knockout, we note that the expression of OR genes, as well as of other axon guidance molecules implicated in OSN axon targeting, were unchanged (fig. S1, H and I). To further probe whether OSN axons expressing the same OR were capable of projecting to their stereotypic positions in the OB, we performed immunohistochemistry (IHC) against the mouse OR m71 (OLFR151) and observed that these OSNs targeted to their predicted positions (Fig. 1H). Consistent with the VGLUT2 staining, m71 glomeruli appeared malformed in OSN-RAD21-cKO mice relative to their OSN-RAD21-het littermates (Fig. 1H). These data are consistent with the established paradigm that Pcdh protein isoform diversity plays a critical role in the assembly of olfactory circuits (*18*–*21*) and suggest that the activity of the cohesin protein complex generates the Pcdh isoform barcoding diversity required for OSN axons to properly converge into glomeruli structures.

Taken together, these data suggest a logic for the regulation of Pcdh promoter choice whereby cohesin activity determines the cellular commitment to either a deterministic and uniform Pcdh barcoding profile (where Pcdh promoter choice is biased toward the enhancer-proximal Pcdhαc2 promoter) or a diverse Pcdh barcoding profile (where Pcdh promoter choice is random and enhancer distance independent).

Developmental regulation of WAPL suggests a model for the generation of Pcdh diversity

We next investigated how cohesin activity could be regulated to drive the developmental switch from the genomic distance–biased expression of Pcdhαc2 to the stochastic expression of all Pcdh genes during OSN maturation. Given the linear arrangement of Pcdh promoters spanning almost 1 Mb of DNA and the location of the transcriptional enhancers (Fig. 1A), we reasoned that the distance that cohesin can traverse along the cluster could determine the probability of Pcdh promoters to be chosen in individual neurons by the enhancers (Fig. 2A). One mechanism known to regulate cohesin processivity on DNA is the activity of the cohesin "unloader" protein WAPL (wings apart–like protein homolog) (*35*–*37*). In the context of the Pcdh gene locus, our model would predict that high WAPL levels would result in frequent unloading of the cohesin complex from DNA and would limit the distance that cohesin can traverse on DNA, therefore restricting the choice to the most enhancer-proximal Pcdh promoters (Fig. 2A). Conversely, low WAPL levels would increase cohesin processivity and promote long-distance cohesin translocation on DNA, therefore allowing the enhancer-distal Pcdh promoters to be chosen.

On the basis of this model, we wondered whether the distinct cell types within the OE express different levels of Wapl and Rad21 mRNAs. We quantified the mRNA levels of Wapl and Rad21 in the different cell types within the OE from our single-cell RNA-seq studies and bulk RNA-seq studies from sorted cells (fig. S2, A and B). Although Rad21 mRNA levels appeared mostly constant across the OE (fig. S2C), we observed a decrease of Wapl mRNA levels that correlated with the onset of stochastic Pcdh expression whereby globose basal cells expressed the highest levels of Wapl mRNA and mOSNs the lowest (Fig. 2B). We found a correlation between the levels of Wapl and the frequency of choice of the Pcdhαc2 promoter in individual cells (Fig. 2C). This correlation agreed with the trajectory of OSN maturation (Fig. 2C).

To visualize this correlation spatially in the OE, we performed RNA fluorescence in situ hybridization (FISH) using probes targeting the mRNA of Wapl, Pcdhαc2, and Omp. We observed that Wapl mRNA levels were highest in the cells closer to the basal layer, where most early OSN precursors reside, and gradually declined toward the apical layer, where most mOSNs reside. This spatial distribution of Wapl mRNA within the OE positively correlated with that of Pcdhαc2 mRNA but negatively correlated with the levels of expression of Omp mRNA (fig. S2D).

Finally, to determine whether WAPL protein levels correlated with its mRNA levels and tissue distribution, we performed IHC in the OE for WAPL and OMP. Consistent with the single-cell RNA-seq and RNA-FISH data, WAPL protein levels decreased as OSNs matured, as evidenced by the loss of staining in the apical side of the OE (Fig. 2D). Unlike WAPL, the levels

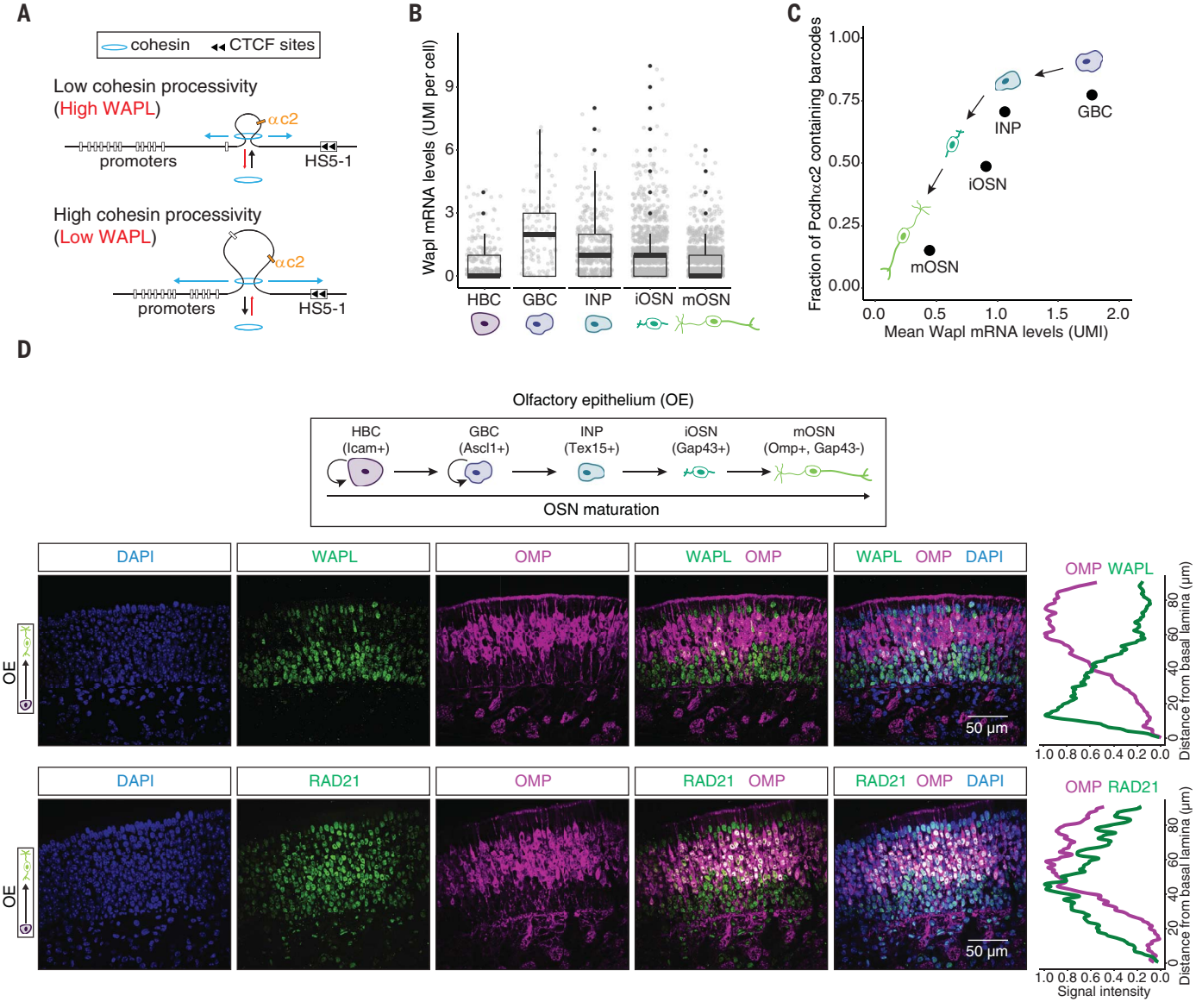

Fig. 2. WAPL is developmentally regulated during OSN maturation. (**A**) Model of WAPL controlling cohesin processivity and thereby defining the probability of choice of Pcdh promoters. (**B**) Quantification of Wapl expression levels from single-cell RNA-seq in distinct cell types of the OE. Dots are individual cells; black line in each box plot is the mean expression level (UMI). (**C**) Fraction of cells in the OE expressing a Pcdhα barcode containing Pcdhαc2 versus mean Wapl mRNA levels. The observed correlation follows the developmental trajectory of OSNs. (**D**) Top: IHC against WAPL and OMP in coronal sections from the OE of OSN-WT mice. Green, WAPL; magenta, OMP; blue, DAPI. Scale bars, 50 μm. Bottom: Same as the top but showing RAD21 levels across the OE. Green, RAD21. For both WAPL and RAD21, quantification of protein levels relative to OMP along the axis of the OE represents the average of two biological replicates.

of the RAD21 protein remained constant throughout the OE (Fig. 2D).

Low WAPL promotes Pcdh isoform diversity in OSNs

To determine whether developmental down-regulation of WAPL in mOSNs promotes Pcdh diversity, we engineered a transgenic mouse line in which we overexpressed WAPL in mOSNs [Omp(tTa);tetO-WAPL-mCherry, OSN-WAPL-XP] and performed both bulk and single-cell RNA-seq (Fig. 3A and fig. S3, A to C). Consistent with our hypothesis, increasing WAPL levels resulted in the biased expression of Pcdhαc2 over the rest of the Pcdhα genes in mOSNs (Fig. 3B), in which under WT conditions, Pcdhα choice is otherwise random and unbiased (Fig. 1B). We also observed a genomic distance–biased expression of the Pcdhγ and Pcdhβ genes (fig. S3D), which resulted in a preferential usage of the Pcdh clusters that correlated with their genomic sizes (Fig. 3C, Pcdhγ > Pcdhα > Pcdhβ). Consistent with these changes in Pcdh expression, Pcdh enhancers displayed genomic distance biases in their contacts with their respective promoters, as assayed by in situ chromatin conformation capture (Hi-C) (Fig. 3D and fig. S3E). These data suggest that high WAPL limits cohesin extrusion along the Pcdh locus, thus favoring the expression of Pcdh promoters located closer, in linear genomic sequence, to their respective enhancers.

If low WAPL levels promote Pcdh isoform diversity in individual neurons, then our model would predict that decreasing WAPL levels below an already low WT level in mOSNs would increase the ability of cohesin to translocate long distances along DNA, thus increasing the probability of choosing promoters that are located farther from their respective enhancers relative to WT.

To test this, we conditionally deleted WAPL in OSNs [Omp(iresCre/+);WAPL$^{fl/fl}$;tdTomato$^{fl/+}$,

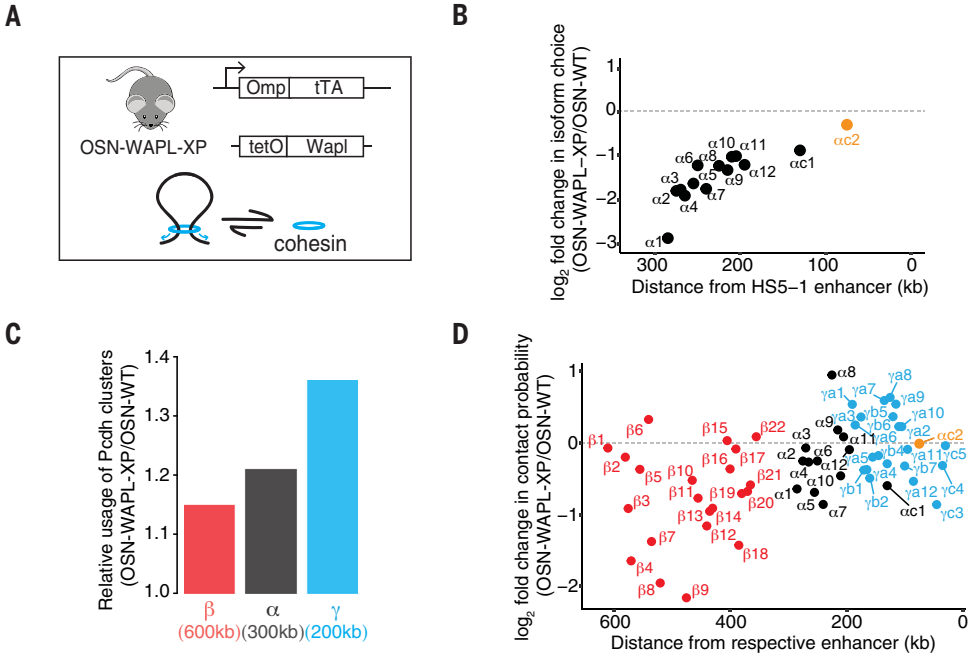

Fig. 3. WAPL overexpression in mature OSNs results in distance-biased Pcdh expression. (**A**) Schematic of the transgenic mouse line used to overexpress WAPL in mOSNs (OSN-WAPL-XP) and its mechanistic prediction. (**B**) Change in Pcdh expression of Pcdhα genes between OSN-WT and OSN-WAPL-XP as a function of the relative distance of their promoters to the HS5-1 enhancer. A total of seven and eight biological replicates of OSN-WT and OSN-WAPL-XP were used. (**C**) Relative usage of Pcdh gene clusters between OSN-WAPL-XP and OSN-WT. The distance between the cluster-specific enhancer to the most distal promoter of that same cluster is shown in parentheses. (**D**) Change in contact probability determined by in situ Hi-C between Pcdh promoters and their respective enhancers as a function of the genomic distance between enhancer-promoter pairs.

OSN-WAPL-cKO] (Fig. 4A and fig. S4, A and B). Consistent with the role of WAPL in regulating cohesin processivity (*35*–*37*), we observed that cohesin enabled a longer reach of the Pcdh enhancers along the cluster in OSN-WAPL-cKO relative to OSN-WT and OSN-RAD21-cKO, as assayed by in situ Hi-C and virtual 4C (Fig. 4B and fig. S4C). We next calculated the contact probability as a function of genomic distance [P(s)] and its derivative to probe the processivity of cohesin. By this metric, cohesin processivity in OSN-WAPL-cKO relative to OSN-WT increased by almost 3-fold (Fig. 4C). We then measured the size of anchored loops and observed a 1.5-fold increase between OSN-WAPL-cKO and OSN-WT (Fig. 4D). Although the P(s) in OSN-WAPL-XP remained mostly unchanged compared with OSN-WT (Fig. 4C), we observed a reduction in the size of anchored loops genome wide (Fig. 4D), consistent with the shorter reach of contacts of Pcdh enhancers with their promoters (Fig. 3D and fig. S3E). Finally, only two anchored loops were detected in OSN-RAD21-cKO (Fig. 4D), consistent with previous studies of cohesin depletion in cells (*38*).

Increasing cohesin processivity on the Pcdh locus by removing WAPL increased the probability of choice of promoters that are located farther from their respective enhancers (Fig. 4E and fig. S4D). These changes scaled with the relative distances of each Pcdh promoter to its enhancer across all three clusters and were consistent with the increased loop sizes observed at the Pcdh locus and genome wide. The distal Pcdhβ promoters, which are located farthest from their respective enhancers (up to 600,000 bp away), had a larger fold change in activation, whereas the Pcdhγ promoters, which are located nearest to their enhancers (up to 200,000 bp away), were the least affected, as assayed by bulk and single-cell RNA-seq (Fig. 4E and fig. S4D). These changes were also evidenced by the mean number of isoforms expressed per cell whereby mOSNs displayed an increase in only the Pcdhβ isoforms in OSN-WAPL-cKO compared with OSN-WT (fig. S4, E and F).

To measure the impact of WAPL levels on Pcdh isoform diversity, we quantified the probability of choice of Pcdh promoters in OSN-WT, OSN-WAPL-XP, and OSN-RAD21-cKO relative to OSN-WAPL-cKO. Increasing WAPL levels resulted in cluster biases in Pcdh diversity that reflected the genomic size of the individual Pcdh gene clusters and the relative distances of their promoters with their respective cluster-specific enhancers (Fig. 4F, Pcdhγ > Pcdhα > Pcdhβ, OSN-WT versus OSN-WAPL-XP). The distance biases in Pcdh isoform diversity that were dependent on WAPL concentration required cohesin activity (Fig. 4F, OSN-RAD21-cKO).

These data indicate that during OSN development, cohesin processivity by WAPL tunes Pcdh isoform diversity and suggest a model for how the deterministic expression of the enhancer-proximal Pcdhαc2 could be favored in other neural types (e.g., in 5-HTs).

High WAPL favors deterministic Pcdhαc2 expression and axon tiling in serotonergic neurons

Unlike OSN axons, which converge, 5-HT axons tile (Fig. 5A). To determine whether Pcdhαc2 expression and axon tiling of 5-HTs require high WAPL, we first investigated whether Wapl mRNA was differentially expressed between 5-HTs and mOSNs. We compared published RNA-seq data from fluorescence-activated cell sorting (FACS)–isolated 5-HT nuclei (*39*) with our RNA-seq data from FACS-isolated mOSNs and found that Wapl expression was ~5-fold higher in 5-HTs compared with mOSNs (Fig. 5B and fig. S5A). To determine whether high WAPL promotes Pcdhαc2 expression, we conditionally removed Wapl in 5-HTs using a Cre driver under the control of the promoter of the serotonin transporter Slc6a4 [Sert(Cre/+); $Wapl^{fl/fl}$;$tdTomato^{fl/+}$, 5-HT-WAPL-cKO] (Fig. 5C, top, and fig. S5B). We then used RNA FISH to measure the levels of Pcdhαc2 mRNA using tryptophan hydroxylase 2 (Tph2) as a marker for serotonergic somas in the raphe. Consistent with our model (Fig. 2A), removal of WAPL resulted in down-regulation of expression of Pcdhαc2 (Fig. 5, C and D).

If high WAPL favors the biased expression of Pcdhαc2 in 5-HTs by promoting low cohesin processivity, then Pcdhαc2 promoter choice should be independent of cohesin activity in these neurons, as we show to be the case in mOSNs (Fig. 1B). To test this, we removed Rad21 in 5-HTs [Sert(Cre/+);$Rad21^{fl/fl}$;$tdTomato^{fl/+}$, 5-HT-RAD21-cKO] (fig. S5C). Consistent with our hypothesis, ablation of Rad21 did not change Pcdhαc2 expression compared with Pcdhαc2 expression in Rad21 heterozygous littermates [Sert(Cre/+);$Rad21^{fl/+}$;$tdTomato^{fl/+}$, 5-HT-RAD21-het] (fig. S5D).

5-HT axons project pervasively from the raphe nuclei through a tiling distribution to several other regions in the brain, including the hippocampus (*14*, *16*). To investigate whether reduced Pcdhαc2 expression upon Wapl deletion results in 5-HT wiring defects, we examined the ability of 5-HT axons to project to the hippocampus (Fig. 5A). We found that 5-HT axons from 5-HT-WAPL-cKO animals presented a clumping phenotype (Fig. 5E) that qualitatively

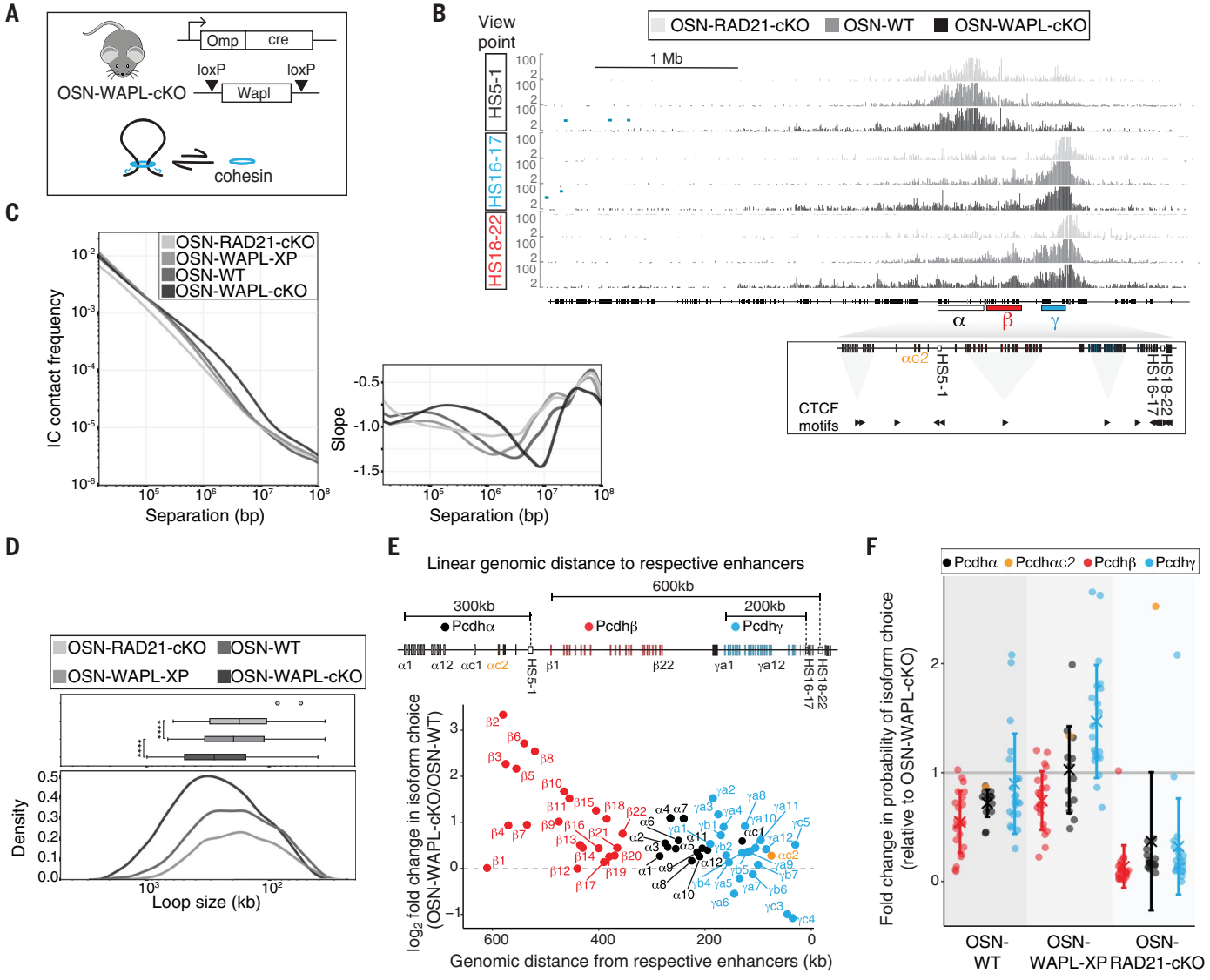

Fig. 4. Ablation of WAPL in mature OSNs results in high cohesin processivity and an increase in Pcdh isoform diversity. (**A**) Schematic of the transgenic mouse line used to conditionally delete WAPL in OSNs (OSN-WAPL-cKO) and its mechanistic prediction. (**B**) Virtual 4C from in situ Hi-C of the chromatin contacts from the HS5-1, the HS16-17, and the HS18-22 enhancers in OSN-RAD21-cKO, OSN-WT, and OSN-WAPL-cKO, respectively. (**C**) Contact frequency as a function of genomic distance (left) and the first derivative (right). Average loop sizes: OSN-RAD21-cKO, not applicable; OSN-WT, 117 kb; OSN-WAPL-XP, 133 kb; and OSN-WAPL-cKO, 333 kb. Results are the average of two biological replicates per genotype. (**D**) Loop anchor distances (corner dots called from in situ Hi-C data) for OSN-RAD21-cKO (two loops), OSN-WAPL-XP (2943 loops, mean loop size of 225 kb), OSN-WT (4820 loops, mean loop size of 262 kb), and OSN-WAPL-cKO (7280 loops, mean loop size of 374 kb). (**E**) Top: Linear genomic distance of Pcdh promoters with respect to their enhancers. Bottom: Log_2-fold change in Pcdh promoter choice calculated by single-cell RNA-seq between OSN-WT and OSN-WAPL-cKO mOSNs as a function of the linear genomic distance of the promoters with respect to their enhancers. (**F**) Quantification of Pcdh isoform diversity. Probability of Pcdh isoform choice in OSN-WT, OSN-WAPL-XP, and OSN-RAD21-cKO relative to OSN-WAPL-cKO. For both (E) and (F), Pcdhα, Pcdhβ, and Pcdhγ genes are shown in black, red, and blue, respectively; Pcdhαc2 is shown in orange.

phenocopied the deletion of the Pcdhαc2 gene (*14*, *16*).

These data suggest that high WAPL in 5-HTs limits cohesin translocation along the Pcdh cluster to promote the biased expression of Pcdhαc2 and 5-HT axon tiling.

Discussion

The generation of cell surface protein isoform diversity as a mechanism to promote neural self-avoidance and axon wiring is a strategy shared across evolution, from invertebrates to vertebrates (*11*). In flies, neurons that require cell surface barcoding diversity for their circuit assembly leverage the massive alternative splicing of the Dscam1 pre-mRNA that alone can generate >18,000 distinct protein isoforms (*40*–*42*). Conversely, neurons that require an identical cell surface barcode to tile harness the Dscam2 gene (*43*), which instead only has two isoforms. By contrast, in mice, the single Pcdh gene locus produces the barcoding programs necessary for different neural wiring patterns, from tiling to convergence (*14*, *18*). Here, we uncovered the molecular logic for how the Pcdh gene cluster achieves transcriptional modularity (Fig. 6). Given the astonishing diversity of neural patterns in the brain and the role that Pcdh proteins play in neural self-avoidance, we propose that different neural types tune cohesin activity, and thereby its processivity, to generate the extent of Pcdh isoform diversity that meets their vastly differing wiring

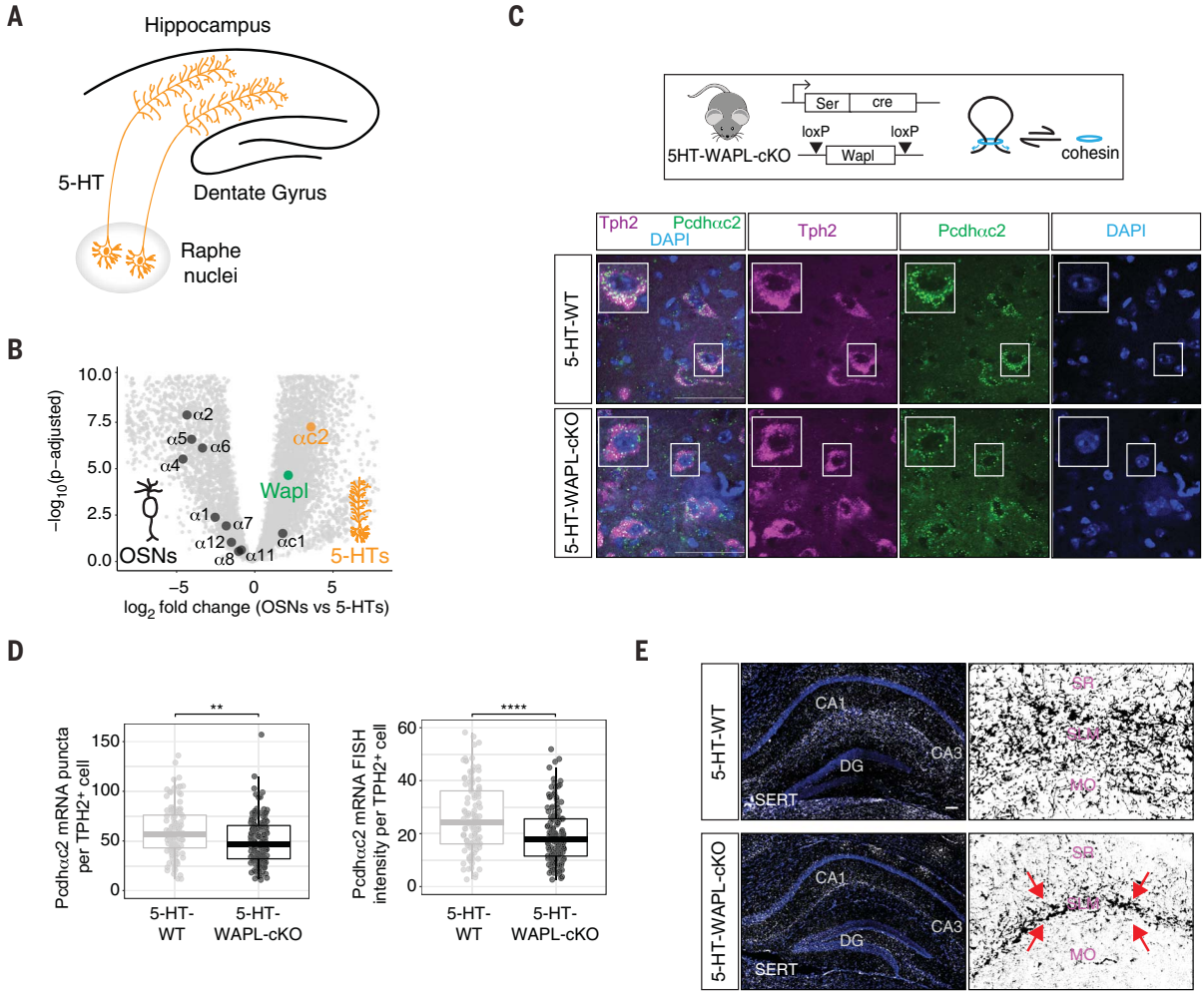

Fig. 5. Ablation of WAPL in 5-HTs results in loss of Pcdhαc2 expression and axon tiling. (**A**) Schematic of 5-HT axon tiling from the raphe to the hippocampus. (**B**) Differential gene expression analysis between OSNs and 5-HTs. Green, Wapl; orange, Pcdhαc2; black, other Pcdhα genes. (**C**) Top: schematic of the transgenic mouse line used to conditionally delete WAPL in 5-HTs (5-HT-WAPL-cKO) and its mechanistic prediction. Bottom: RNA-FISH in the raphe in 5-HT-WT and 5-HT-WAPL-cKO mice. Magenta, Tph2; green, Pcdhαc2; blue, DAPI. Scale bars, 50 μm. (**D**) Quantification of the number of puncta (left) and signal intensity (right) of Pcdhαc2 mRNA in Tph2$^+$ cells in 5-HT-WT and 5-HT-WAPL-cKO 5-HTs. Each dot represents data from an individual Tph2$^+$ cell, with two biological replicates per condition. (**E**) 5-HT wiring defects in 5-HT-WAPLcKO mice relative to 5-HT-WT. Left: 5-HTs are indicated by IHC against SERT. White, SERT; blue, DAPI. CA1, cornu ammonis 1; CA3, cornu ammonis 3; DG, dentate gyrus. Right: Binary mask of SERT signal in presented images. SR, stratum radiatum; SLM, stratum lacunosum moleculare; MO, molecular layer. Red arrows indicate clumping of 5-HT axons. Scale bar, 100 μm.

requirements. We uncovered WAPL as a key modulator of Pcdh isoform diversity (Fig. 6). However, given the many cohesin subunits and known protein regulators, we speculate that other mechanisms might exist, beyond that of modulating WAPL levels, that define the combinatorial space of Pcdh isoform diversity.

In support of this proposal, there are several observations that implicate genetic variants of the cohesin protein complex and its regulators associated with cohesinopathies, including Cornelia de Lange syndrome and Roberts syndrome (*44*), with dysregulation of Pcdh expression. It was found that clustered Pcdh genes are down-regulated in cells derived from Cornelia de Lange syndrome patients (*45*), in NIPBL (a cohesin loader)–heterozygous mouse models of Cornelia de Lange Syndrome (*46*), and in brains isolated from the cohesin-STAG1 core subunit null embryos (*47*). On the basis of these observations and the data presented here, it is reasonable to speculate that the severe intellectual impairments associated with cohesinopathies arise from the dysregulation of clustered Pcdh expression. Thus, the implications of our findings extend beyond the mechanism of regulating healthy brain development and establish a biochemical ground between the genetic variants of the cohesin protein complex and Pcdh dysregulation. More broadly, we also wonder whether our proposed model could provide a molecular framework for the recently suggested link among cohesin, 3D genome structure, maturation, and function of mouse cortical neurons that extends beyond the regulation of Pcdh gene expression (*48*, *49*).

Rheostats as strategies to overcome transcriptional biases and achieve stochasticity of genes arranged in clusters

We revealed an activity of the cohesin protein complex and its unloader, WAPL, in the diversification of cell surface proteomes required for brain wiring. Aspects of our proposed mechanism extend beyond the Pcdh gene locus and apply more generally to the regulation of other gene clusters with expression programs that are required for cellular diversification and fate. There is precedence for such a process in B cells, which also control their cohesin activity through WAPL to maximize antibody diversity using V(D)J recombination during

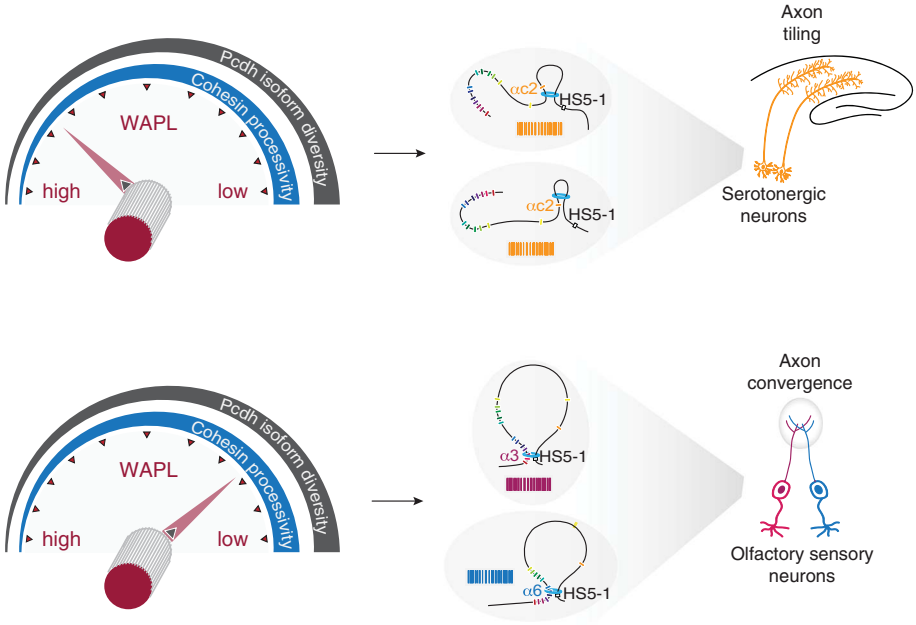

Fig. 6. Model: WAPL functions as a rheostat of cohesin processivity and Pcdh isoform diversity that regulates neural wiring patterns. High WAPL limits cohesin extrusion through the Pcdh locus, favoring the choice of Pcdh promoters that are located closer to their enhancers. In 5-HTs, high WAPL favors the choice of the sole Pcdhαc2 promoter, thus constraining 5-HT axon wiring to a tiling pattern. As WAPL levels decrease, cohesin processivity increases. Cohesin extrusion through the Pcdh locus erases genomic distance biases in Pcdh promoter choice by the distal enhancers. Therefore, as WAPL levels decrease, Pcdh isoform diversity increases. In OSNs, low WAPL favors stochastic Pcdh promoter choice independent of enhancer-promoter distance, a mechanism that generates sufficient Pcdh protein isoform diversity required for convergence of OSN axons. Only Pcdhα genes (rainbow colors with Pcdhαc2 in orange) are shown. Blue, cohesin; red, WAPL rheostat. Barcodes correspond to the colors of the Pcdhα isoform chosen.

maturation (*50*, *51*). In that context, cohesin promotes contraction of the mouse immunoglobulin locus to facilitate random contacts between the V_H genes and the recombined DJH segments by the recombination center located at the 3′ end of the locus (*51*). Also in this context, WAPL has been proposed to regulate the distance that cohesin can extrude along the immunoglobulin locus to maximize antibody diversification (*50*, *51*). These observations suggest a rheostat-like function of WAPL also in the regulation of V(D)J recombination and antibody diversity.

In addition, there is a parallel in the logic of promoter stochasticity between Pcdh genes and OR genes. In fact, single OR choice in OSNs necessitates the anatomically regulated rheostatic-like activity of the NFIA, B, and X transcription factors that regulate the gradient of heterochromatin assembly and genome compartmentalization along the dorsoventral axis of the OE to promote zonal OR promoter choice (*52*). Our studies suggest that proper assembly of olfactory maps requires the developmental regulation of yet another rheostat, that of WAPL, which enables Pcdh diversity in mOSNs by controlling cohesin processivity on the Pcdh locus.

On the basis of these previous studies and our present results, we propose that a rheostat-operating logic is used by cells to enable promoter stochasticity in gene clusters, the architectures of which demand mechanisms to overcome transcriptional biases. Given that rheostat-operating mechanisms might require large changes in the concentration of protein factors with activity that is also essential for cell division (*53*), as is the case for WAPL, we hypothesize that the use of such strategies could be confined to noncycling cells such as B cells and postmitotic neurons.

Materials and methods

Animals

Mice were treated in compliance with the rules and regulations of the institutional animal care and use committee under protocol number AN-170364-03F. For all experimental procedures performed in OSNs, both male and female animals between 3 and 24 weeks of age were used. For experiments performed to investigate Pcdh expression in 5-HTs, both male and female animals between 2 and 4 weeks of age were used. Primary FACS-sorted cells were obtained from dissected main OE. OSNs were sorted from Omp(iresGFP/+) mice. Rad21 cKO OSNs were achieved as described previously (*24*). Briefly, Rad21 conditional allele mice were crossed to Omp(iresCre/+) mice ($Omp^{tm1(cre)Jae}$). Recombined cells were purified by including a Cre-inducible tdTomato allele [ROSA26-tdtomato, $Gt(ROSA)26Sor^{tm14(CAG-tdTomato)Hze/J}$] in the cross and selecting $tdTomato^+$ cells by FACS. In the text and the figures, we refer to the Rad21 cKO in OSNs as OSN-RAD21-cKO for homozygous deletion of the floxed allele and as OSN-RAD21-het for heterozygous deletion of the floxed allele. The WAPL-overexpressing mouse was obtained by microinjection of a linearized DNA plasmid containing the tetO-WAPL-mCherry cassette using the Gladstone mouse facility core at the University of California San Francisco (UCSF). A total of four transgenic founders were characterized with two to three biological replicates each. When crossed to Omp(tTa) mice, WAPL-overexpressing OSNs were sorted using mCherry. The WAPL conditional allele mouse was generated as described previously (*54*). WAPL floxed mice were crossed to Omp(iresCre/+) or to Sert(Cre) (JAX strain 014554) mice to conditionally delete WAPL in OSNs or 5-HTs, respectively. In the text and the figures, we refer to the WAPL cKO as OSN-WAPL-cKO and 5-HT-WAPL-cKO for homozygous deletion of the floxed allele in OSNs and 5-HTs, respectively. Primers used for genotyping are listed in table S1.

FACS sorting of mouse OSNs

Cells were dissociated into a single-cell suspension by incubating freshly dissected main OE with papain for 30 to 40 min at 37°C according to the Worthington Papain Dissociation System. After dissociation and filtering through a 35-μm cell strainer, cells were resuspended in 1× phosphate-buffered saline (PBS) with 2% fetal bovine serum (FBS) with DNase (0.0025% final concentration) and 4′,6-diamidino-2-phenylindole (DAPI). For in situ Hi-C experiments, upon dissociation, cells were fixed with 1% formaldehyde for 10 min at room temperature (RT). Formaldehyde was quenched by adding glycine to a final concentration of 0.125 M for 5 min at RT. Cells were then washed once and resuspended in cold PBS with 2% FBS and DNase (0.0025% final concentration). Fluorescent cells were then sorted on a FACSAria II cell sorter (BD Biosciences).

RNA isolation and sequencing studies

RNA was isolated from tissue using TRIzol. Cell lysate was extracted with bromo-chloropropane, and RNA was precipitated with 100% isopropanol supplemented with 10 μg of glycoblue for 10 min at RT and then pelleted at 16,000*g* for 30 min at 4°C. The RNA pellet was washed once with 75% ethanol and then resuspended in RNase-free water to a maximal concentration of 200 ng/μl. Genomic DNA contaminants were removed by Turbo DNase. Removal of Turbo

DNase was performed by phenol:chloroform extraction, and RNA was precipitated as described above, resuspended in RNase-free water, and stored at −80°C.

Sequencing libraries for total RNA were made using the SMARTer Stranded Total RNA-Seq Pico input mammalian RNA kit v2. The quality and quantity of all libraries were assessed by Bioanalyzer and Qubit. Libraries were sequenced on a NextSeq 500/550 (UCSF Gladstone Genomic Core). Unless otherwise stated, RNA-seq data represent two biological replicates per condition.

Single-cell RNA-seq studies

Cells were dissociated from the main OE from 8- to 12-week-old female mice as described above. About 16,000 cells were FACS purified for OSNs, submitted for 10x Genomics GEM generation using the Single Cell 5′ Gene Expression set-up, and sequenced using a NovaSeq SP100 PE50 (UCSF Gladstone Genomic Core and the UCSF Center for Advanced Technology) and a NextSeq2000 P2 200. The data were analyzed using 10x Genomics Cell Ranger 6.0.1 with a recovery of 4000 to 8000 cells per experiment. Data analysis was performed using Seurat (*55*–*58*) and custom scripts. Pcdh isoform choice in mOSNs was defined as the detection of UMI-corrected reads in cells of high Omp expression (Omp^+, $Gap43^-$). Single-cell RNA-seq analysis and statistics are provided in table S2. Data for single-cell experiments represent one biological replicate per condition.

In situ Hi-C

About 500,000 sorted OSNs were lysed and intact nuclei were processed through an in situ Hi-C protocol as previously described with a few modifications (*59*). Briefly, cells were lysed with lysis buffer [50 mM Tris, pH 7.5, 0.5% igepal, 0.25% sodium deoxycholate, 0.1% sodium dodecyl sulfate (SDS), 150 mM NaCl, and protease inhibitors]. Pelleted intact nuclei were then resuspended in 0.5% SDS and incubated for 20 min at 65°C for nuclear permeabilization. After quenching with 1.1% Triton-X for 10 min at 37°C, nuclei were digested with 6 U/μl of DpnII in 1x DpnII buffer overnight at 37°C. After the initial digestion, a second DpnII digestion was performed at 37°C for 2 hours. DpnII was heat-inactivated at 65°C for 20 min. For the 1.5 hours fill-in at 37°C, biotinylated dATP (Jena Bioscience) was used instead of dATP to increase ligation efficiency. Ligation was performed at 25°C for 4 hours. Nuclei were then pelleted and sonicated in sonication buffer (10 mM Tris pH 7.5, 1 mM EDTA, 0.25% SDS) on a Covaris S220 (peak power 105.0; duty factor 2.0; cycle/burst 200; treatment time 960 s; temperature 4 to 8°C). DNA was reverse cross-linked overnight at 65°C with proteinase K and RNAse A. Reverse cross-linked DNA was purified with 2× AMPure beads following the standard protocol. Biotinylated fragments were enriched using Dynabeads MyOne Streptavidin T1 beads. The biotinylated DNA fragments were prepared for next-generation sequencing on the beads by using the Nugen Ovation Ultralow kit protocol with some modifications. After end repair, magnetic beads were washed twice at 55°C with 0.05% Tween, 1 M NaCl in Tris/EDTA, pH 7.5. Residual detergent was removed by washing the beads twice in 10 mM Tris, pH 7.5. End repair buffers were replenished to original concentrations, but the enzyme and enhancer was omitted before adapter ligation. After adapter ligation, beads underwent five washes with 0.05% Tween, 1 M NaCl in Tris/EDTA, pH 7.5, at 55°C and two washes with 10 mM Tris, pH 7.5. DNA was amplified by 10 cycles of polymerase chain reaction irrespective of starting material. Beads were reclaimed, and amplified DNA fragments were purified with 0.8× AMPure beads. The OSN-WAPL-cKO and OSN-WAPL-XP Hi-C datasets were generated using the Arima Hi-C kit according to the manufacturer's instructions. Quality and concentration of libraries were assessed by Agilent Bioanalyzer and Qubit. Samples were paired-end sequenced on a NextSeq 550 and 2000 and a NovaSeq (UCSF Gladstone Genomic Core and the UCSF Center for Advanced Technology). Hi-C analysis and statistics are provided in table S3. For OSN-WAPL-XP, two Hi-C biological replicates were performed using cells FAC sorted from seven and five animals per replicate. For OSN-WAPL-cKO, two Hi-C biological replicates were performed using cells FAC sorted from one animal per replicate.

Bioinformatic analysis of sequencing data

For RNA-seq experiments, raw FASTQ files were aligned with STAR using the mm10 reference genome. The initial four base pairs of both paired reads were trimmed before alignment. Differential expression analysis was performed using DESeq2 (*60*). When comparing OSNs and 5-HTs, seven biological replicates from FACS-isolated OSNs and three published datasets from FACS-isolated raphe nuclei from 5-HTs were used (*39*). When comparing OSN-WT with OSN-RAD21-cKO, OSN-RAD21-het, OSN-WAPL-XP, or OSN-WAPL-cKO, seven biological replicates from FACS-isolated OSN-WT, two biological replicates from FACS-isolated OSN-RAD21-cKO and OSN-RAD21-het, eight biological replicates from FACS-isolated OSN-WAPL-XP, and two biological replicates from FACS-isolated OSN-WAPL-cKO were used.

For in situ Hi-C experiments, raw FASTQ files were processed using HiC-Pro (*61*, *62*) (table S3). The Hi-C maps were generated from raw Hi-C matrices in the cooler format by binning valid pairs into 5-kb bins. Raw matrices for the two replicates were merged (using cooler merge) and iteratively corrected (using cooler balance) (*63*). The normalized matrices were then smoothed and interpolated for visualization (using cooltools adaptive_coarsegrain and interp_nan, https://doi.org/10.5281/zenodo.5214125). The contact probability as a function of genomic separation P(s) was computed using cooltools.expected_cis. Loop sizes were estimated based on the position of the peak in the log-derivative of P(s), with a correction factor equal to 0.6 according to (*64*). Anchored loops were called using Mustache (*65*) on the balanced cool files of two merged Hi-C replicates binned at 5-kb resolution. The threshold P value for an interaction to be reported was set at 0.05 (using option −pt). Distances between anchors were computed based on the midpoints of the anchor coordinates.

Preparation of mouse brain tissue sections

Animals were perfused using standard transcardial perfusion with ice-cold PBS and 4% paraformaldehyde (PFA), and brain tissue was immediately dissected. For experiments using OE and OB tissues, the OE/OB were dissected and immersion fixed in 4% PFA for 8 min, washed in PBS for 5 min three times at RT and incubated in 30% sucrose overnight at 4°C. The following day, samples were incubated in a 1:1 30% sucrose and optimal cutting temperature (OCT) solution for 1 hour and then moved to OCT for 1 hour before freezing. Samples were frozen in embedding molds using isopropanol and dry ice. For experiments targeting 5-HT neurons in the raphe and hippocampus, whole brains were dissected and placed in 4% PFA overnight at 4°C. The brains were then washed in PBS for 5 min three times at RT and transferred to 30% sucrose at 4°C overnight. Once sunk, OB tissue was removed from 30% sucrose, incubated in a tube containing a 1:1 solution of 30% sucrose and OCT embedding compound (Sakura, #4583) for 1 hour at RT, followed by another hour of RT incubation in an embedding mold containing pure OCT. Whole brains, once sunk, were directly transferred from 30% sucrose solution to an embedding mold containing 2:1 30% sucrose and OCT. To freeze the tissue in its embedding solution, the mold was flash frozen in dry ice and isopropanol. Tissue was stored at −80°C until sectioning. Samples in OCT were placed in a Leica cryostat (Leica Microsystems, Wetzlar, Germany) for 30 to 45 min before sectioning to equilibrate. OCT was used to freeze samples to cryostat chucks. Sectioning was performed with a chamber temperature of −21°C and an object temperature of −17°C. Samples were sectioned coronally at 16 μm (OE and OB) and at 20 μm (hippocampus and raphe). All sections were mounted onto Superfrost Plus slides (Fisher Scientific, #12-550-15) and stored at −20°C until downstream use.

Immunohistochemistry

For immunostaining of OB tissue, sections were fixed with 4% PFA in PBS, washed for 5 min three times with PBS containing 0.1% Triton X-100, and blocked in 4% donkey serum in PBS plus 0.1% Triton X-100 for 30 min at RT. For immunostaining of the hippocampus region, sections were directly washed with PBS plus 0.1% Triton X-100 and incubated with the same blocking serum for 30 min at RT. After the blocking step, the slides were incubated in a humid chamber with primary antibodies diluted in blocking serum for 24 hours at 4°C. The following primary antibodies were used: rabbit anti-SERT (1:500, Millipore Sigma, #PC177L100UL), guinea pig anti-VgGLUT2 (1:2000, Millipore Sigma, #AB2251-I), guinea pig anti-m71 (1:1000, from the laboratory of G. Barnea), rabbit anti-WAPL (1:400, Invitrogen, #MA5-38145), rabbit anti-RAD21 (1:100, Invitrogen, #PA528344), goat anti-OMP (1:1000, Fujifilm Wako Chemicals, #544-10001), and rabbit anti-GAP43 (1:500, Abcam, #ab75810). After extensive washing with PBS plus 0.1% Triton X-100, sections were incubated with Alexa Fluor–conjugated secondary antibodies diluted in blocking serum for 2 hours before being washed again and mounted with Vectashield Antifade Mounting Medium with DAPI (Vector Laboratories). Alexa Fluor 488 donkey immunoglobulin G (IgG) anti-rabbit (1:2000, Invitrogen, #A21206), and Alexa Fluor 647 goat anti–guinea pig IgG (1:2000, Invitrogen, #A21450) were used as secondary antibodies. For all immunohistochemistry experiments, at least two biological replicates were characterized, and representative images are shown.

Hybridization chain reaction experiments on fixed tissue sections

RNA-FISH experiments were performed using hybridization chain reaction (HCR) technology from Molecular Instruments. Fixed tissue sections from postnatal day 20 mice were stored at −20°C and allowed to dry at RT for 5 min. An HCR protocol (dx.doi.org/10.17504/protocols.io.8epv59725g1b/v2) was then performed. The following probes and matching hairpins ordered from Molecular Instruments were used: Tph2 (lot number PRE854), Pcdhαc2 (lot number PRK987), Omp (lot number PRK986), and Wapl (lot number PRQ058). The hairpin amplification systems used for Tph2 and Pcdhαc2 were B1 at 647 nm and B3 at 488 nm, respectively. The B4 546-nm hairpin amplification system was used for both Omp and Wapl.

Imaging studies

Sections from the OB and raphe were imaged using a Yokogawa CSU-W1 SoRa spinning disk confocal microscope. Sections from the hippocampus were imaged using a Leica DMi8 inverted microscope and stitched using the LAS X software platform. All images were postprocessed in Fiji software.

Quantification of Pcdhαc2 expression in the raphe nuclei

Pcdhαc2 and Wapl mRNA expression levels in individual 5-HT neurons were quantified using a custom CellProfiler pipeline (*66*). The pipeline categorized input images from HCR experiments into groups of three as follows: (i) images containing Pcdhαc2 or Wapl mRNA signal, (ii) images containing the Tph2 mRNA signal, and (iii) manual segmentations of 5-HT somas based on Tph2 expression performed in Fiji. The pipeline first identified 5-HT somas from the manual segmentations using the two-class Otsu thresholding method with a correction factor of 1.0. These somas were then used as a mask over the Pcdhαc2/Wapl images, only keeping signal residing within 5-HT somas. The masked Pcdhαc2/Wapl images were then enhanced for speckle features with a maximum size of 10 pixels to make mRNA puncta easier to identify. Pcdhαc2 and Wapl puncta were identified using the robust background thresholding method with a correction factor of 1.0, lower and upper outlier fractions of 0.05, and 3 SDs for Pcdhαc2 images. Five SDs were used for Wapl images to account for the slightly lower signal-to-noise ratio generated by the Wapl probes relative to the Pcdhαc2 probes. Clumped puncta were distinguished by shape, and dividing lines between clumped objects were drawn based on intensity. Finally, the RelateObjects module was used to assign Pcdhαc2 and Wapl puncta to their parent 5-HT somas. Data for all Pcdhαc2 and Wapl puncta and Tph2 soma objects were exported using the ExportToSpreadsheet module. To quantify Pcdhαc2 and Wapl mRNA abundance, both the number of puncta in $Tph2^{+}$ somas and the total intensity of all puncta within a soma were measured. Both metrics agreed on the reported effects on Pcdhαc2 and Wapl expression.

To determine sample size for experiments comparing Pcdhαc2 and Wapl expression in 5-HT neurons, the number of cells required to have an 80% power, at probability level 0.05, of detecting a difference of 10 puncta per cell between an experimental condition and a control condition with a mean of 60 puncta per cell was calculated, with both conditions having SDs of 20 puncta. Our calculations estimated 65 cells per condition, and between 65 and 140 cells per condition from two biological replicates were used in each experiment. The mean and SD values were determined from pilot experiments in WT tissue.

Quantification of IHC and RNA-FISH signal in the OE

For quantification of IHC images, signal intensity profiles were generated in Fiji and averaged across three biological replicates. WAPL, RAD21, and OMP signals were quantified using equally sized rectangular selections spanning from the basal lamina of the OE to the apical sustentacular cell layer. For quantification of RNA-FISH signal, Pcdhαc2, Wapl, and Omp puncta were identified using the same CellProfiler pipeline as described above. Two images were quantified for each mRNA, with each being from a different biological replicate. In each of these images, a line was manually drawn in Fiji outlining the basal lamina of the OE. These lines were exported as a series of (x,y) coordinates. For each punctum identified in the CellProfiler pipeline, the shortest distance was calculated between the punctum and the basal lamina using the punctum's (x,y) coordinates and the coordinates of the basal line. These distances were plotted as histograms with 25 bins for each RNA.

Quantification and statistics

Statistical tests were performed using two-sided Wilcoxon rank-sum tests. Statistically significant effects are reported in the respective figure panels using asterisks as $^{*}P < 0.05$, $^{**}P < 0.01$, $^{***}P < 0.001$, and $^{****}P < 0.0001$; otherwise, the P values associated with the observed transcriptional changes are provided in Figure 5B.

REFERENCES AND NOTES

1. N. Maizels, Immunoglobulin gene diversification. *Annu. Rev. Genet.* **39**, 23–46 (2005). doi: 10.1146/annurev.genet.39.073003.110544; pmid: 16285851
2. K. Monahan, S. Lomvardas, Monoallelic expression of olfactory receptors. *Annu. Rev. Cell Dev. Biol.* **31**, 721–740 (2015). doi: 10.1146/annurev-cellbio-100814-125308; pmid: 26359778
3. G. Mountoufaris, D. Canzio, C. L. Nwakeze, W. V. Chen, T. Maniatis, Writing, Reading, and Translating the Clustered Protocadherin Cell Surface Recognition Code for Neural Circuit Assembly. *Annu. Rev. Cell Dev. Biol.* **34**, 471–493 (2018). doi: 10.1146/annurev-cellbio-100616-060701; pmid: 30296392
4. K. Monahan, A. Horta, S. Lomvardas, LHX2- and LDB1-mediated trans interactions regulate olfactory receptor choice. *Nature* **565**, 448–453 (2019). doi: 10.1038/s41586-018-0845-0; pmid: 30626972
5. Q. Wu, T. Maniatis, A striking organization of a large family of human neural cadherin-like cell adhesion genes. *Cell* **97**, 779–790 (1999). doi: 10.1016/S0092-8674(00)80789-8; pmid: 10380929
6. Q. Wu, T. Maniatis, Large exons encoding multiple ectodomains are a characteristic feature of protocadherin genes. *Proc. Natl. Acad. Sci. U.S.A.* **97**, 3124–3129 (2000). doi: 10.1073/pnas.97.7.3124; pmid: 10716726
7. S. Yokota *et al*., Identification of the cluster control region for the protocadherin-beta genes located beyond the protocadherin-gamma cluster. *J. Biol. Chem.* **286**, 31885–31895 (2011). doi: 10.1074/jbc.M111.245605; pmid: 21771796
8. P. Kehayova, K. Monahan, W. Chen, T. Maniatis, Regulatory elements required for the activation and repression of the protocadherin-α gene cluster. *Proc. Natl. Acad. Sci. U.S.A.* **108**, 17195–17200 (2011). doi: 10.1073/pnas.1114357108; pmid: 21949399
9. D. Canzio, T. Maniatis, The generation of a protocadherin cell-surface recognition code for neural circuit assembly. *Curr. Opin. Neurobiol.* **59**, 213–220 (2019). doi: 10.1016/j.conb.2019.10.001; pmid: 31710891
10. J. L. Lefebvre, Neuronal territory formation by the atypical cadherins and clustered protocadherins. *Semin. Cell Dev. Biol.* **69**, 111–121 (2017). doi: 10.1016/j.semcdb.2017.07.040; pmid: 28756270
11. S. L. Zipursky, W. B. Grueber, The molecular basis of self-avoidance. *Annu. Rev. Neurosci.* **36**, 547–568 (2013). doi: 10.1146/annurev-neuro-062111-150414; pmid: 23841842
12. S. L. Zipursky, J. R. Sanes, Chemoaffinity revisited: Dscams, protocadherins, and neural circuit assembly. *Cell* **143**, 343–353 (2010). doi: 10.1016/j.cell.2010.10.009; pmid: 21029858

13. J. L. Lefebvre, J. R. Sanes, J. N. Kay, Development of dendritic form and function. *Annu. Rev. Cell Dev. Biol.* **31**, 741–777 (2015). doi: 10.1146/annurev-cellbio-100913-013020; pmid: 26422333
14. W. V. Chen *et al*., Pcdhαc2 is required for axonal tiling and assembly of serotonergic circuitries in mice. *Science* **356**, 406–411 (2017). doi: 10.1126/science.aal3231; pmid: 28450636
15. S. Katori *et al*., Protocadherin-alpha family is required for serotonergic projections to appropriately innervate target brain areas. *J. Neurosci.* **29**, 9137–9147 (2009). doi: 10.1523/JNEUROSCI.5478-08.2009; pmid: 19625505
16. S. Katori *et al*., Protocadherin-αC2 is required for diffuse projections of serotonergic axons. *Sci. Rep.* **7**, 15908 (2017). doi: 10.1038/s41598-017-16120-y; pmid: 29162883
17. J. L. Lefebvre, D. Kostadinov, W. V. Chen, T. Maniatis, J. R. Sanes, Protocadherins mediate dendritic self-avoidance in the mammalian nervous system. *Nature* **488**, 517–521 (2012). doi: 10.1038/nature11305; pmid: 22842903
18. G. Mountoufaris *et al*., Multicluster Pcdh diversity is required for mouse olfactory neural circuit assembly. *Science* **356**, 411–414 (2017). doi: 10.1126/science.aai8801; pmid: 28450637
19. S. Hasegawa *et al*., The protocadherin-α family is involved in axonal coalescence of olfactory sensory neurons into glomeruli of the olfactory bulb in mouse. *Mol. Cell. Neurosci.* **38**, 66–79 (2008). doi: 10.1016/j.mcn.2008.01.016; pmid: 18353676
20. S. Hasegawa *et al*., Constitutively expressed protocadherin-α regulates the coalescence and elimination of homotypic olfactory axons through its cytoplasmic region. *Front. Mol. Neurosci.* **5**, 97 (2012). doi: 10.3389/fnmol.2012.00097; pmid: 23087612
21. S. Hasegawa *et al*., Distinct and cooperative functions for the *protocadherin*-α, -β and -γ clusters in neuronal survival and axon targeting. *Front. Mol. Neurosci.* **9**, 155 (2016). doi: 10.3389/fnmol.2016.00155; pmid: 28066179
22. B. Tasic *et al*., Promoter choice determines splice site selection in protocadherin alpha and gamma pre-mRNA splicing. *Mol. Cell* **10**, 21–33 (2002). doi: 10.1016/S1097-2765(02)00578-6; pmid: 12150904
23. X. Wang, H. Su, A. Bradley, Molecular mechanisms governing Pcdh-γ gene expression: Evidence for a multiple promoter and cis-alternative splicing model. *Genes Dev.* **16**, 1890–1905 (2002). doi: 10.1101/gad.1004802; pmid: 12154121
24. D. Canzio *et al*., Antisense lncRNA transcription mediates DNA demethylation to drive stochastic protocadherin α promoter choice. *Cell* **177**, 639–653.e15 (2019). doi: 10.1016/j.cell.2019.03.008; pmid: 30955885
25. Y. Guo *et al*., CTCF/cohesin-mediated DNA looping is required for protocadherin α promoter choice. *Proc. Natl. Acad. Sci. U.S.A.* **109**, 21081–21086 (2012). doi: 10.1073/pnas.1219280110; pmid: 23204437
26. Y. Guo *et al*., CRISPR inversion of CTCF sites alters genome topology and enhancer/promoter function. *Cell* **162**, 900–910 (2015). doi: 10.1016/j.cell.2015.07.038; pmid: 26276636
27. K. Monahan *et al*., Role of CCCTC binding factor (CTCF) and cohesin in the generation of single-cell diversity of protocadherin-α gene expression. *Proc. Natl. Acad. Sci. U.S.A.* **109**, 9125–9130 (2012). doi: 10.1073/pnas.1205074109; pmid: 22550178
28. Z. Jia *et al*., Tandem CTCF sites function as insulators to balance spatial chromatin contacts and topological enhancer-promoter selection. *Genome Biol.* **21**, 75 (2020). doi: 10.1186/s13059-020-01984-7; pmid: 32293525
29. M. Merkenschlager, E. P. Nora, CTCF and cohesin in genome folding and transcriptional gene regulation. *Annu. Rev. Genomics Hum. Genet.* **17**, 17–43 (2016). doi: 10.1146/annurev-genom-083115-022339; pmid: 27089971
30. G. Fudenberg *et al*., Formation of chromosomal domains by loop extrusion. *Cell Rep.* **15**, 2038–2049 (2016). doi: 10.1016/j.celrep.2016.04.085; pmid: 27210764
31. E. Alipour, J. F. Marko, Self-organization of domain structures by DNA-loop-extruding enzymes. *Nucleic Acids Res.* **40**, 11202–11212 (2012). doi: 10.1093/nar/gks925; pmid: 23074191
32. A. L. Sanborn *et al*., Chromatin extrusion explains key features of loop and domain formation in wild-type and engineered genomes. *Proc. Natl. Acad. Sci. U.S.A.* **112**, E6456–E6465 (2015). doi: 10.1073/pnas.1518552112; pmid: 26499245
33. K. J. Ressler, S. L. Sullivan, L. B. Buck, Information coding in the olfactory system: Evidence for a stereotyped and highly organized epitope map in the olfactory bulb. *Cell* **79**, 1245–1255 (1994). doi: 10.1016/0092-8674(94)90015-9; pmid: 7528109
34. F. Wang, A. Nemes, M. Mendelsohn, R. Axel, Odorant receptors govern the formation of a precise topographic map. *Cell* **93**, 47–60 (1998). doi: 10.1016/S0092-8674(00)81145-9; pmid: 9546391
35. S. Kueng *et al*., Wapl controls the dynamic association of cohesin with chromatin. *Cell* **127**, 955–967 (2006). doi: 10.1016/j.cell.2006.09.040; pmid: 17113138
36. G. Wutz *et al*., Topologically associating domains and chromatin loops depend on cohesin and are regulated by CTCF, WAPL, and PDS5 proteins. *EMBO J.* **36**, 3573–3599 (2017). doi: 10.15252/embj.201798004; pmid: 29217591
37. J. H. I. Haarhuis *et al*., The cohesin release factor WAPL restricts chromatin loop extension. *Cell* **169**, 693–707.e14 (2017). doi: 10.1016/j.cell.2017.04.013; pmid: 28475897
38. S. S. P. Rao *et al*., Cohesin loss eliminates all loop domains. *Cell* **171**, 305–320.e24 (2017). doi: 10.1016/j.cell.2017.09.026; pmid: 28985562
39. E. Södersten *et al*., A comprehensive map coupling histone modifications with gene regulation in adult dopaminergic and serotonergic neurons. *Nat. Commun.* **9**, 1226 (2018). doi: 10.1038/s41467-018-03538-9; pmid: 29581424
40. D. Hattori *et al*., Dscam diversity is essential for neuronal wiring and self-recognition. *Nature* **449**, 223–227 (2007). doi: 10.1038/nature06099; pmid: 17851526
41. B. J. Matthews *et al*., Dendrite self-avoidance is controlled by Dscam. *Cell* **129**, 593–604 (2007). doi: 10.1016/j.cell.2007.04.013; pmid: 17482551
42. W. M. Wojtowicz, J. J. Flanagan, S. S. Millard, S. L. Zipursky, J. C. Clemens, Alternative splicing of *Drosophila* Dscam generates axon guidance receptors that exhibit isoform-specific homophilic binding. *Cell* **118**, 619–633 (2004). doi: 10.1016/j.cell.2004.08.021; pmid: 15339666
43. S. S. Millard, J. J. Flanagan, K. S. Pappu, W. Wu, S. L. Zipursky, Dscam2 mediates axonal tiling in the *Drosophila* visual system. *Nature* **447**, 720–724 (2007). doi: 10.1038/nature05855; pmid: 17554308
44. E. Watrin, F. J. Kaiser, K. S. Wendt, Gene regulation and chromatin organization: Relevance of cohesin mutations to human disease. *Curr. Opin. Genet. Dev.* **37**, 59–66 (2016). doi: 10.1016/j.gde.2015.12.004; pmid: 26821365
45. P. Garcia *et al*., Disruption of NIPBL/Scc2 in Cornelia de Lange Syndrome provokes cohesin genome-wide redistribution with an impact in the transcriptome. *Nat. Commun.* **12**, 4551 (2021). doi: 10.1038/s41467-021-24808-z; pmid: 34315879
46. S. Kawauchi *et al*., Multiple organ system defects and transcriptional dysregulation in the Nipbl(+/-) mouse, a model of Cornelia de Lange syndrome. *PLOS Genet.* **5**, e1000650 (2009). doi: 10.1371/journal.pgen.1000650; pmid: 19763162
47. S. Remeseiro, A. Cuadrado, G. Gómez-López, D. G. Pisano, A. Losada, A unique role of cohesin-SA1 in gene regulation and development. *EMBO J.* **31**, 2090–2102 (2012). doi: 10.1038/emboj.2012.60; pmid: 22415368
48. Y. Fujita *et al*., Decreased cohesin in the brain leads to defective synapse development and anxiety-related behavior. *J. Exp. Med.* **214**, 1431–1452 (2017). doi: 10.1084/jem.20161517; pmid: 28408410
49. L. Calderon *et al*., Cohesin-dependence of neuronal gene expression relates to chromatin loop length. *eLife* **11**, e76539 (2022). doi: 10.7554/eLife.76539; pmid: 35471149
50. L. Hill *et al*., Wapl repression by Pax5 promotes V gene recombination by Igh loop extrusion. *Nature* **584**, 142–147 (2020). doi: 10.1038/s41586-020-2454-y; pmid: 32612238
51. H.-Q. Dai *et al*., Loop extrusion mediates physiological Igh locus contraction for RAG scanning. *Nature* **590**, 338–343 (2021). doi: 10.1038/s41586-020-03121-7; pmid: 33442057
52. E. Bashkirova *et al*., Homeotic regulation of olfactory receptor choice via NFI-dependent heterochromatic silencing and genomic compartmentalization. bioRxiv 274035 [Preprint] (2020); https://doi.org/10.1101/2020.08.30.274035.
53. I. F. Davidson, J.-M. Peters, Genome folding through loop extrusion by SMC complexes. *Nat. Rev. Mol. Cell Biol.* **22**, 445–464 (2021). doi: 10.1038/s41580-021-00349-7; pmid: 33767413
54. A. Tedeschi *et al*., Wapl is an essential regulator of chromatin structure and chromosome segregation. *Nature* **501**, 564–568 (2013). doi: 10.1038/nature12471; pmid: 23975099
55. Y. Hao *et al*., Integrated analysis of multimodal single-cell data. *Cell* **184**, 3573–3587.e29 (2021). doi: 10.1016/j.cell.2021.04.048; pmid: 34062119
56. T. Stuart *et al*., Comprehensive integration of single-cell data. *Cell* **177**, 1888–1902.e21 (2019). doi: 10.1016/j.cell.2019.05.031; pmid: 31178118
57. A. Butler, P. Hoffman, P. Smibert, E. Papalexi, R. Satija, Integrating single-cell transcriptomic data across different conditions, technologies, and species. *Nat. Biotechnol.* **36**, 411–420 (2018). doi: 10.1038/nbt.4096; pmid: 29608179
58. R. Satija, J. A. Farrell, D. Gennert, A. F. Schier, A. Regev, Spatial reconstruction of single-cell gene expression data. *Nat. Biotechnol.* **33**, 495–502 (2015). doi: 10.1038/nbt.3192; pmid: 25867923
59. S. S. P. Rao *et al*., A 3D map of the human genome at kilobase resolution reveals principles of chromatin looping. *Cell* **159**, 1665–1680 (2014). doi: 10.1016/j.cell.2014.11.021; pmid: 25497547
60. M. I. Love, W. Huber, S. Anders, Moderated estimation of fold change and dispersion for RNA-seq data with DESeq2. *Genome Biol.* **15**, 550 (2014). doi: 10.1186/s13059-014-0550-8; pmid: 25516281
61. N. Servant *et al*., HiC-Pro: An optimized and flexible pipeline for Hi-C data processing. *Genome Biol.* **16**, 259 (2015). doi: 10.1186/s13059-015-0831-x; pmid: 26619908
62. R. H. van der Weide *et al*., Hi-C analyses with GENOVA: A case study with cohesin variants. *NAR Genom. Bioinform.* **3**, lqab040 (2021). doi: 10.1093/nargab/lqab040; pmid: 34046591
63. N. Abdennur, L. A. Mirny, Cooler: Scalable storage for Hi-C data and other genomically labeled arrays. *Bioinformatics* **36**, 311–316 (2020). doi: 10.1093/bioinformatics/btz540; pmid: 31290943
64. K. Polovnikov, B. Slavov, S. Belan, M. Imakaev, H. B. Brandão, L. A. Mirny, Crumpled polymer with loops recapitulates key features of chromosome organization. bioRxiv 478588 [Preprint] (2023); https://doi.org/10.1101/2022.02.01.478588.
65. A. Roayaei Ardakany, H. T. Gezer, S. Lonardi, F. Ay, Mustache: Multi-scale detection of chromatin loops from Hi-C and Micro-C maps using scale-space representation. *Genome Biol.* **21**, 256 (2020). doi: 10.1186/s13059-020-02167-0; pmid: 32998764
66. A. E. Carpenter *et al*., CellProfiler: Image analysis software for identifying and quantifying cell phenotypes. *Genome Biol.* **7**, R100–R111 (2006). doi: 10.1186/gb-2006-7-10-r100; pmid: 17076895
67. L. Kiefer *et al*., WAPL functions as a rheostat of Protocadherin isoform diversity that controls neural wiring (2023), doi: 10.5281/zenodo.7613545

ACKNOWLEDGMENTS

We thank T. Maniatis, S. Lomvardas, G. Narlikar, E. Nora, H. Madhani, V. Ramani, M. Paredes, G. Mountoufaris, E. Cannavo, H. Shayya, and members of the Canzio and Nora laboratories for helpful discussions and suggestions; J.-M. Peters for the generous gift of the Wapl$^{(fl/fl)}$ mouse; G. Barnea for the antibody for the olfactory receptor m71; the UCSF Gladstone Mouse Transgenic Core for help in the generation of transgenic animals; M. Bernardi and H.-R. Lin of the Gladstone Genomics Core for assistance with bulk and single-cell sequencing experiments; and S. Kim and the staff of the UCSF Center for Advanced Light Microscopy for support with image acquisition and analysis. **Funding:** This work was supported by the National Institute of General Medicine (grant R00 GM121815-05 to D.C.); the National Institute of Mental Health (grant DP2 MH129955-01 to D.C.); a CZ Biohub Investigator grant (D.C.); and the National Science Foundation (graduate research fellowship grant 2034836 to A.B.). Any opinions, findings, and conclusions, or recommendations expressed in this material are those of the authors and do not necessarily reflect the views of the National Science Foundation. **Authors contributions:** D.C. and L.K. conceived the project. L.K. designed, performed, and interpreted the bulk of the genomic experiments. A.C. and A.B. designed, performed, and interpreted the studies in 5-HT. J.L. designed, performed, and interpreted the IHC studies in the OB. S.G. helped with the analysis and interpretation of the in situ Hi-C data. G.I.F.S. and S.M.R. established the initial protocols to perform genomic experiments in OSNs with help from E.S.C.. A.H. helped with the establishment of the in situ Hi-C protocols. A.V. and A.J. assisted with immunohistochemistry studies and mouse genotyping. M.H.M. assisted with mouse colony management. D.C. supervised the project and wrote the paper with substantial help from L.K., A.C., A.B., J.L., and S.G. **Competing interests:** The authors declare no competing interests. **Data and materials availability:** All data are available in the main text or the supplementary materials, and all reagents can be made available from the corresponding author upon request. Source data have been deposited in NCBI's Gene Expression Omnibus and are accessible through GEO series accession number GSE191195. Custom scripts can be found at Zenodo (67).

SUPPLEMENTARY MATERIALS

science.org/doi/10.1126/science.adf8440
Figs. S1 to S5
Tables S1 to S3
MDAR Reproducibility Checklist

View/request a protocol for this paper from *Bio-protocol*.

Submitted 17 November 2022; accepted 7 May 2023
10.1126/science.adf8440

WAPL functions as a rheostat of Protocadherin isoform diversity that controls neural wiring

Lea Kiefer, Anna Chiosso, Jennifer Langen, Alex Buckley, Simon Gaudin, Sandy M. Rajkumar, Gabrielle Isabelle F. Servito, Elizabeth S. Cha, Akshara Vijay, Albert Yeung, Adan Horta, Michael H. Mui, and Daniele Canzio

Science, **380** (6651), eadf8440.
DOI: 10.1126/science.adf8440

Editor's summary
Neural self-nonself discrimination requires the generation of cell surface "barcoding" diversity. Neurons expressing the same barcode avoid each other to maximize interactions with other neurons. In mammals, clustered Protocadherin (Pcdh) proteins function as barcodes. By studying the expression regulation of Pcdh genes in mouse serotonergic and olfactory sensory neurons, Kiefer *et al*. uncovered that the combinatorial space of Pcdh isoform diversity in individual cells rests on the DNA translocation activity of cohesin and its unloader, WAPL. These findings expand the repertoire of molecular logic that generates the protein isoform diversity required for cell fate and function. —Di Jiang